ACS NANO

www.acsnano.org

ARTICLE

Distance and Voltage Dependence of Orbital Density Imaging Using a CO-Functionalized Tip in Scanning Tunneling Microscopy

Fabian Paschke,[#] Leonard-Alexander Lieske,[#] Florian Albrecht, C. Julian Chen, Jascha Repp, and Leo Gross*

Cite This: https://doi.org/10.1021/acsnano.4c14476

Read Online

ACCESS | Metrics & More | Article Recommendations | Supporting Information

ABSTRACT: The appearance of frontier molecular ion resonances measured with scanning tunneling microscopy (STM)—often referred to as orbital density images—of single molecules was investigated using a CO-functionalized tip in dependence on bias voltage and tip−sample distance. As model systems, we studied pentacene and naphthalocyanine on bilayer NaCl on Cu(111). Absolute tip−sample distances were determined by means of atomic force microscopy (AFM). STM imaging revealed a transition from predominant *p*- to *s*-wave tip contrast upon increasing the tip−sample distance, but the contrast showed only small changes as a function of voltage. The distance-dependent contrast change is explained with the steeper decay of the tunneling matrix element for tunneling between two *p*-wave centers, compared to tunneling between two *s*-wave centers. In simulations with a fixed ratio of *s*- to *p*-wave tip states, we can reproduce the experimental data including the distance-dependent transition from predominant *p*- to *s*-wave tunneling contribution.

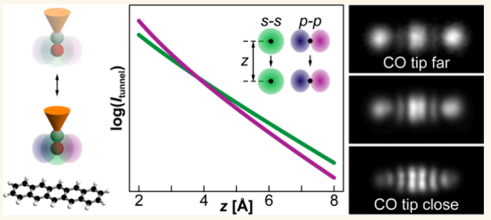

KEYWORDS: *scanning tunneling microscopy, CO-tip functionalization, single molecules, atomic force microscopy, Bardeen's tunneling theory, density functional theory*

Recent progress in on-surface synthesis[1−4] enabled the generation of elusive and long-sought molecules, as for example graphene nanoribbons,[5] high-spin hydrocarbons,[6−9] elusive molecular allotropes of carbon,[10−14] nanographenes,[15−19] and molecules with open-shell[20−22] or antiaromatic character.[23,24] In addition, chemical reactions were explored using atom manipulation, for example, retro-Bergman reactions[25] and selective redox reactions.[26] Investigation of elusive products and the determination of their properties crucially relies on AFM and STM to reveal their geometric and electronic structures, respectively. The imaging of molecular orbital densities by STM, often performed on ultrathin NaCl layers,[27] can reveal intriguing properties and effects, such as hydrogen tautomerization,[28] metal-molecule bond formation,[29,30] Jahn−Teller distortions,[26,31,32] entanglement of multireference states,[33] or switching between open- and closed-shell configurations.[34] In many cases, CO-tip functionalization is the method of choice to enhance the spatial resolution in both AFM[35] and STM.[36] However, the interpretation of the CO-tip STM contrast, in particular by comparison to calculated molecular orbitals, is not straightforward because CO tips have not only an *s*-wave character, but in addition a *p*-wave character. It has been shown that the contribution of *p*-wave character in CO-tip STM varies both with tip−sample distance[37−44] and with bias voltage.[45]

Orbital density images obtained by STM are typically assigned to the attachment (detachment) of electrons to (from) frontier molecular orbitals.[27] Using a metallic STM tip with tip states of mainly *s*-wave character,[38] such images resemble the electron density related to the probed orbital, which we refer to as *s*-wave tip contrast. Attaching a CO molecule at the tip apex introduces tip wave functions that derive from the $2\pi^*$-states of CO,[36,46] having *p*-wave character with a nodal plane perpendicular to the sample surface. The $2\pi^*$-states of CO come as degenerate pairs, which have p_x- and p_y-orbital character with x and y being the two Cartesian coordinates in the surface plane. According to Chen's derivative rule,[47] tunneling *via* such *p*-wave tip states results in images that show the squared modulus of the lateral gradient of the sample's wave function, which we name a *p*-wave tip contrast.[36] A CO tip comprises both *s*- and *p*-wave tip states, which can be approximated by *s*- and *p*-wave states localized at

Received: October 14, 2024
Revised: December 10, 2024
Accepted: December 20, 2024
Published: January 8, 2025

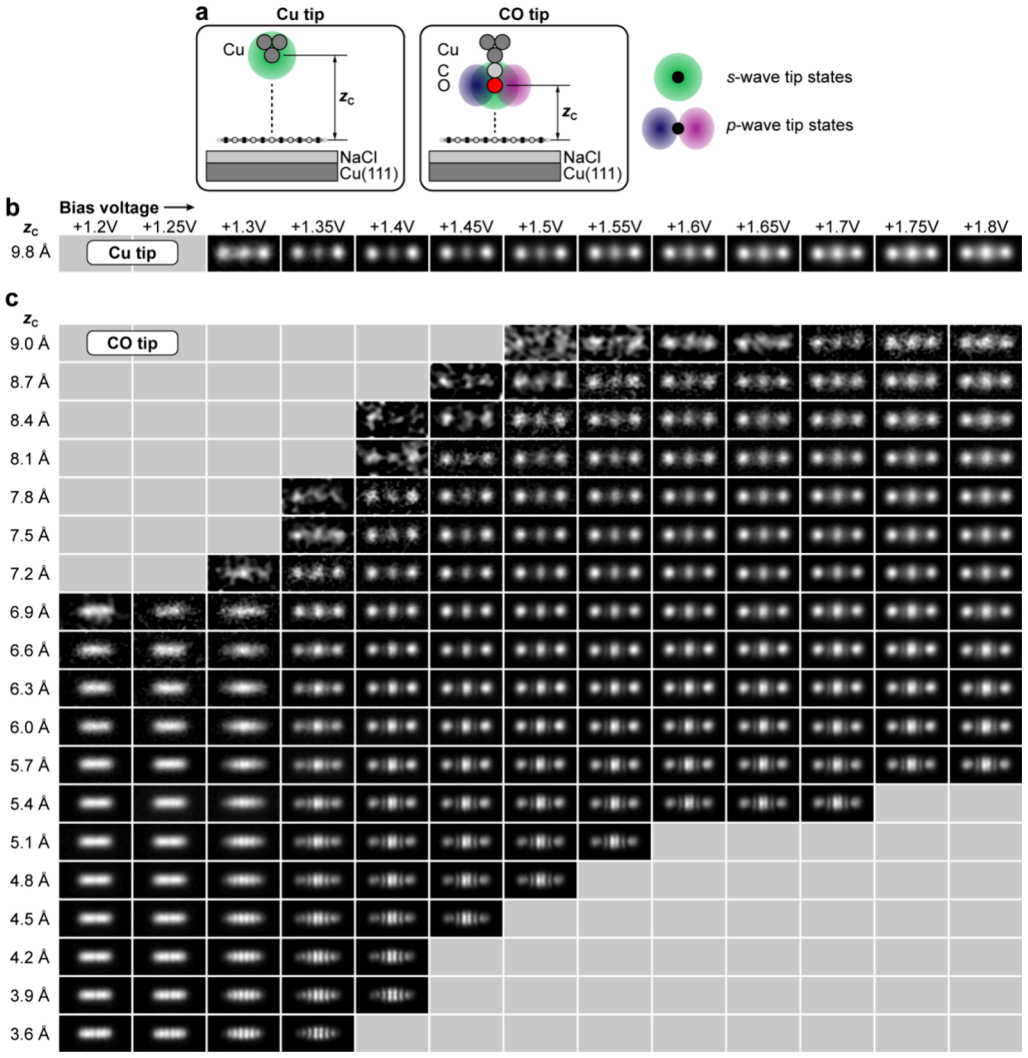

Figure 1. Distance- and voltage-dependent contrast at the NIR with a Cu tip and a CO-functionalized tip. (a) Sketch of the experiment. The absolute tip−sample distances z_C for both Cu and CO tips were calibrated by AFM using the same tips as for the respective STM measurements (see Figure S1). *s*- and *p*-wave tip states are schematically drawn to the respective foremost tip atom. (b) Constant-height STM data recorded with a Cu tip at z_C = 9.8 Å, at bias voltages from the resonance onset (V = +1.3 V) across the NIR. Data obtained at different z_C are plotted in Figure S4. (c) Constant-height STM data recorded with a CO tip for different bias voltages V across the NIR (horizontal) and different tip−sample distances z_C (vertical). Gray panels are in regions at which the tunneling current I was below the detection limit (I < 0.01 pA, top left) and in regions where the tunneling current became too large for stable imaging (I > 100−300 pA, bottom right). Each color scale ranges from zero (black) to the respective maximum current I_{max} (white), see Figure S4 for I_{max} values. Image sizes 3.0 nm × 1.5 nm.

the oxygen atom,[44,46] and a mixed *s*- and *p*-wave tip contrast has been observed in STM experiments.[36,39,41,42,45,48−50] Furthermore, experiments have shown that the CO-tip STM contrast nontrivially relies on the imaging parameters: A relative increase in *s*-wave tip contrast has been observed both with increased tip−sample distance[38−41,44] and with an increased absolute value of the bias voltage.[45] Our work aims to provide an experimentally backed up explanation of the tip-height dependence and voltage dependence of CO-tip orbital density STM images, to evaluate these dependencies in quantitative terms, and to advance their understanding and modeling.

Here, we systematically investigate the distance and voltage dependence of CO-tip STM. We resolve the transition from *p*-wave to *s*-wave tip contrast upon increasing the tip−sample distance and reproduce it by calculating the different decay constants of the respective tunneling matrix elements. We employ AFM to quantify absolute tip−sample distances. In simulations, with a fixed ratio of *s*- to *p*-wave tip states, we obtain good agreement for all measured tip heights and provide explanations for the observed contrast changes. Our findings facilitate the comparison of CO-tip STM images with calculated molecular orbitals.

RESULTS/DISCUSSION

As model compounds, we investigated individual pentacene[27,29,36] and naphthalocyanine[28,36] molecules adsorbed on bilayer NaCl on a Cu(111) surface with metal (Cu) and CO-functionalized STM tips.[51] AFM $\Delta f(z)$ spectroscopy was used to calibrate the tip−sample distance (see Methods and Figure S1).[52,53] The calibrated, absolute tip−sample distance z_C refers to the distance between the center of the foremost tip atom and the molecular plane of the imaged molecule, see Figure 1a.

https://doi.org/10.1021/acsnano.4c14476
ACS Nano XXXX, XXX, XXX−XXX

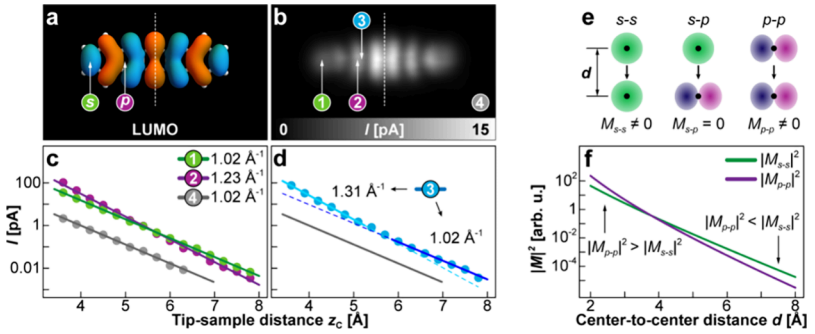

Figure 2. $I(z)$ spectroscopy with a CO tip. (a) Calculated LUMO of pentacene plotted at an isovalue of 0.01 e/a_{Bohr}^3. Local *s*- and *p*-like sites are indicated. (b) Constant-height STM data recorded at the NIR (V = +1.35 V, z_C = 4.5 Å) of pentacene on bilayer NaCl/Cu(111) using a CO tip. Sites of $I(z_C)$ spectroscopy are indicated. Dotted lines in (a) and (b) denote the short center axis of the molecule as a guide to the eye. Image size 3.0 nm × 1.5 nm. (c) $I(z_C)$ obtained from the data set shown in Figure 1c at V = +1.35 V, at positions 1 (local *s*-like site), 2 (local *p*-like site), and 4 (bare substrate), see (b). Solid lines: single exponential fits to the data, with the tunneling decay constants κ indicated. (d) $I(z_C)$ at position 3 (neither *s*- nor *p*-like site). The data is fitted by two separate fits for z_C = [3; 5.3] Å (light blue) and z_C = [6; 8] Å (dark blue). Extrapolations are plotted as dashed lines and a gray line denotes the fit on NaCl as shown in (c). (e, f) Calculated distance dependence of the tunneling matrix element $|M|^2$ between two vertically aligned *s*-centers (green) and *p*-centers (purple), see Methods. *d* denotes their center-to-center distance.

On bilayer NaCl, pentacene exhibits ion resonances around sample bias voltages V of V = −2.3 V (positive ion resonance, PIR) and V = +1.6 V (negative ion resonance, NIR).[27] In the main text, we focus the discussion on the NIR (see Figures S2 and S3 and Supplementary Note 1 for respective data at the PIR and corresponding discussion). To systematically investigate the evolution of the STM contrast, we collected a series of constant-height STM images as a function of both tip−sample distance z_C and sample bias V, see Figure 1b,c.

Figure 1b displays data obtained with a Cu-terminated (*s*-wave) tip. The images at the NIR (V > +1.3 V) exhibit three intense lobes, as reported previously.[27] Upon increasing V beyond the onset of the NIR, we observe a subtle intensity increase of the central lobe with respect to the end lobes. We do not observe a pronounced distance dependence with the Cu tip for 7.4 Å < z_C < 10.4 Å; hence, we here display data only for a single value of z_C (different distances are shown in Figure S4).

Measurements performed with a CO tip are displayed in Figure 1c. At all probed bias voltages V beyond the onset of the NIR (V = +1.35 V to V = +1.8 V), the STM contrast exhibits a strong distance dependence. For small z_C (z_C < 4 Å), the contrast is dominated by six maxima, corresponding to a pronounced *p*-wave tip contrast.[36] Going to an intermediate z_C (z_C ≈ 5.7 Å), the relative intensity at the molecular center and both ends increases. For large z_C (z_C > 7 Å), the images resemble the measurements obtained with the Cu (*s*-wave) tip (Figure 1b), that is, three lobes, with the central lobe gaining intensity with respect to the end lobes upon increasing V beyond the onset of the NIR.

The lowest unoccupied molecular orbital (LUMO) of pentacene exhibits local *s*- and *p*-like sites, *i.e.*, maxima and nodal planes between two adjacent maxima, respectively, see Figure 2a. For different lateral positions shown in Figure 2b, we extract current-versus-distance spectra $I(z_C)$ from the STM data at V = +1.35 V and plot the results in Figure 2c,d. Fitting the $I(z_C)$ data obtained at site 1 (local *s*-like site), site 2 (local *p*-like site), and site 4 (on the bare NaCl surface) by single-exponentials $I(z) \approx I_0 e^{-2\kappa z}$,[54] we obtain the tunneling decay constants $\kappa_{1(s)}$, $\kappa_{2(p)}$, and $\kappa_{4(NaCl)}$. The decay at the *p*-like site $\kappa_{2(p)}$ = 1.23 ± 0.02 Å^{-1} (purple in Figure 2c) is steeper compared to the *s*-like site $\kappa_{1(s)}$ = 1.02 ± 0.01 Å^{-1} (green in Figure 2c) and the bare NaCl substrate $\kappa_{4(NaCl)}$ = 1.02 ± 0.02 Å^{-1} (gray in Figure 2c). In addition, compared to the *s*-like site and bare NaCl site, we observe that at the *p*-like site, the fit by a single exponential is less good. The experimental log(I)-versus-z_C data of the *p*-like site shows a positive curvature, indicating that the decay constant decreases with increasing z_C. If we fit the data on the *p*-like site by two exponentials, we obtain $\kappa_{2(p)}^{close}$ = 1.35 ± 0.02 Å^{-1} fitting only the "close" interval [3; 5.3] Å and $\kappa_{2(p)}^{far}$ = 1.13 ± 0.06 Å^{-1} fitting only the "far" interval [6; 8] Å (see Figure S5). Note that in the "close" interval, the decay is steeper than in the "far" interval, but even in the "far" interval, the decay is still steeper compared to the *s*-like site.

Fitting the data on site 3, which is neither a local *s*- nor *p*-like site, by two exponentials, we obtain κ_3^{close} = 1.31 ± 0.02 Å^{-1} and κ_3^{far} = 1.02 ± 0.02 Å^{-1} (Figure 2d). That is, in the "close" interval, the decay corresponds to the value obtained at the *p*-like site, and in the "far" interval, the decay corresponds to the value obtained at the *s*-like site. With a Cu tip, we obtained decay constants of $\kappa_{Cu\text{-}tip} \approx$ 0.95 ± 0.02 Å^{-1}, with small variation at different lateral sites across the molecule, see Figure S6.

The different observed decay constants can be explained within the framework of Bardeen's tunneling theory,[55,56] under the assumption that a CO tip exhibits both *s*- and *p*-wave tip states.[46] As wave functions, we employ spherical vacuum wave functions[47] (see Methods) with an identical decay constant λ for *s*- and *p*-centers (note that we denote decay constants of wave functions by λ, but decay constants of tunneling current and tunneling matrix elements by κ). We calculated the tunneling matrix elements $M_{i\text{-}j}$ between two vertically aligned *s*- and *p*-centers, respectively, representing elastic tunneling between tip (subscript i) and sample (subscript j) states, see Figure 2e. Note that the tunneling matrix element between vertically aligned *s*- and *p*-centers is zero ($M_{s\text{-}p}$ = 0).[36] The tunneling current I is proportional to the squared modulus of M, *i.e.*, $I \propto |M|^2$, which is displayed in Figure 2f as a function of distance between the two centers. Although the vacuum decay constants λ of wave functions of the *s*- and *p*-centers are identical, Figure 2f shows that the tunneling matrix element between two *p*-wave centers $|M_{p\text{-}p}|^2$ is subject to a steeper decay constant κ than the one between two *s*-wave centers,

https://doi.org/10.1021/acsnano.4c14476
ACS Nano XXXX, XXX, XXX−XXX

i.e., $|M_{s\text{-}s}|^2$.[37,39,40,45,57]. We provided an intuitive explanation for this behavior in Figure S7 and Supplementary Note 2. In addition, $\log(|M_{p\text{-}p}|^2)$ exhibits a positive curvature with a steeper decay at smaller tip−sample distances compared to larger tip−sample distances. The calculated distance dependences of $|M_{s\text{-}s}|^2$ and $|M_{p\text{-}p}|^2$ qualitatively resemble the measured $I(z_C)$ data obtained on the *s*- and *p*-like sites (Figure 2c and Figure S5).

Based on this agreement, we suggest that transport above *s*-wave sites is predominated by tunneling from CO-tip *s*-wave states (e.g., at position 1), but at *p*-wave sites from CO-tip *p*-wave states (e.g., at position 2). Other sites can be expanded in different multipole contributions, hence as a superposition of *s*- and *p*-like sites (see Methods). Higher-order multipole contributions such as *d*-like sites are not considered here. The sum of $|M_{s\text{-}s}|^2$ and $|M_{p\text{-}p}|^2$ contributions exhibits a crossover between a *z*-range predominated by $|M_{p\text{-}p}|^2$ (at small tip−sample distance) and a *z*-range predominated by $|M_{s\text{-}s}|^2$ (at large tip−sample distance), see Figure 2f. This agrees well with the $I(z_C)$ data obtained on site 3 (Figure 2d), which suggests that at sites of combined *s*- and *p*-like character, tunneling *via* the CO-tip *p*-wave states predominates at small tip−sample distances, while tunneling *via* *s*-wave states predominates at large tip−sample distances. Note that in this picture, the tip height z_C' at which the crossover from dominating $|M_{p\text{-}p}|^2$ contribution toward dominating $|M_{s\text{-}s}|^2$ contribution occurs, will depend on the relative contributions of *s*- and *p*-like character at the respective site. That is, the larger the relative local *p*-like (*s*-like) character in the orbital density, the larger (smaller) the crossover-distance z_C'.

A site-dependent tunneling decay also explains the evolution of CO-tip STM image contrast as a function of distance, as observed in Figure 1c. For small z_C (z_C < 4 Å), tunneling *via* CO-tip *p*-wave states predominates the current (at almost all lateral positions), which creates the dominant *p*-wave tip contrast at small distances.[36] At an intermediate z_C ($z_C \approx 5.7$ Å), the tunneling current contributions through *s*- and *p*-wave tip states are overall of comparable magnitude. However, the relative contributions of tunneling *via* *s*- and *p*-wave tip states will be different at different lateral positions. Above sites with similar *s*- and *p*-like character they might be similar, whereas above sites of local *s*-wave (*p*-wave) character, tunneling *via* *s*-wave (*p*-wave) tip states will predominate. The STM contrast thus reflects a superposition of *s*- and *p*-wave tip contrast, which has been observed previously in CO-tip STM experiments.[36,39,41,42,45,48−50] For large z_C (z_C > 7 Å), tunneling *via* CO-tip *s*-wave states predominates the current (at almost all lateral positions), and the STM contrast resembles the Cu (*s*-wave) tip measurements (Figure 1b).

The origin of the particular *s*-wave tip contrast of the STM image at the NIR, comprising three prominent lobes, is twofold. First, the large tip−sample distance (z_C > 7 Å) leads to a decrease of the lateral resolution such that only the two outermost and the central lobe remain visible (Figure S8).[27,58] Note that with a Cu tip, imaging at z_C < 7 Å is not possible because the tunneling currents become too large for stable imaging. However, with a less conductive, pentacene-terminated tip, all seven lobes of the LUMO were resolved.[27] Second, pentacene's outermost benzene rings bend toward the NaCl surface, affecting the relative intensity of the lobes at the ends with respect to the lobe at the center.[59] We observe almost no spatial variation of $\kappa_{Cu\text{-}tip}$ across the molecule (Figure S6d), in line with the absence of a pronounced distance dependence in the Cu-tip STM contrast (Figure S4a). Small intramolecular differences of $\kappa_{Cu\text{-}tip}$ at different lateral positions above the molecule as well as a substantially decreased $\kappa_{Cu\text{-}tip} \approx 0.8–0.9$ Å^{-1} above the perimeter of the molecule (Figure S6) can be explained by topographical considerations.[60]

While elastic tunneling with different κ involving *s*- and *p*-wave tip states accounts for the pronounced distance dependence, it does not explain the subtle voltage-dependent contrast variations. In images with dominating *s*-wave tip contrast (Cu tip: Figure 1b; CO tip: Figure 1c, z_C > 7 Å), we observe a relative intensity increase in the central lobe when increasing *V* across the NIR (*V* = +1.35 V to *V* = +1.8 V). This finding can be explained by electron−vibron (e−ν) coupling in the framework of an extended Franck−Condon (FC) model.[61] In the FC picture, the excess energy of tunneling electrons (with respect to the resonance onset, here at *V* = +1.35 V) excites vibrational modes in the molecule. This electron-vibron coupling can lead to the opening of additional tunneling channels (vibration-assisted tunneling), for which the tunneling matrix elements can couple tip and sample states of different symmetry.[45,61,62] For an *s*-wave (*p*-wave) tip, this effect results in a growing contribution of *p*-wave (*s*-wave) tip contrast upon increasing *V* above the onset of the resonance. For a metal *s*-wave tip, the effect has been shown to be more pronounced above the center of pentacene, where the LUMO has a high density of nodal planes, facilitating e−ν coupling.[45] We thus expect that, for tips and distances at which an *s*-wave tip contrast is predominating, the increased e−ν coupling in the central region of pentacene is responsible for the relative increase of the central lobe with increasing voltage. These arguments explain the voltage dependence of the Cu-tip STM contrast (Figure 1b) and of the CO-tip STM contrast for large distances (Figure 1c, z_C > 7 Å).

We do not observe a pronounced voltage dependence in CO-tip STM at intermediate distances (Figure 1c, $z_C \approx 5.7$ Å). At these tip heights, elastic tunneling through both *s*- and *p*-wave tip states already contributes to the contrast significantly, as explained above. Adding inelastic contributions from e−ν coupling for a tip that already has a mixed character seems to not change the contrast substantially. For CO-tip STM at small distances (Figure 1c, $z_C \lesssim 5$ Å), at which the image at the onset of the resonance is predominated by *p*-wave tip contrast, one might expect increasing *s*-wave tip contrast at voltages exceeding the onset of the resonance due to e−ν coupling. However, this regime could not be probed, because the resulting tunneling currents become too large for stable imaging (bottom right area of Figure 1c).

Next, we discuss the distance-dependent transition from *p*- to *s*-wave tip contrast in STM images for the case of pentacene by comparing experimental (Figure 3a) to simulated (Figure 3b) STM images at the NIR. Accompanying AFM measurements allowed us to calibrate the tip−sample distance z_C in absolute terms,[52,53] as described in Figure S1. Consequently, the tip heights used for the simulations (z_{sim}) are not fitting parameters but have been fixed to the experimentally determined, calibrated values z_C. For the CO-tip states, we used a fixed *s*/*p*-ratio of 2.5/1 (corresponding to the prefactors of the tip wave functions) with wave functions centered at the foremost atom (oxygen),[44] see Methods for more details. The resulting STM images reproduce the experimental findings well over the explored *z*-range (Figure 3), showing a transition from *p*-wave STM contrast to *s*-wave contrast with increasing

https://doi.org/10.1021/acsnano.4c14476
ACS Nano XXXX, XXX, XXX−XXX

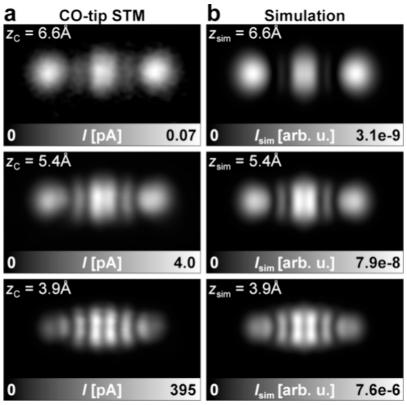

Figure 3. Comparison of STM measurement and simulation. (a) Constant-height CO-tip STM data at the NIR (V = +1.4 V) of pentacene on bilayer NaCl/Cu(111) at different z_C indicated in each panel. (b) Simulated constant-height STM images of the NIR of pentacene adsorbed on NaCl. The simulations were performed at the AFM calibrated tip−sample distances $z_{sim} = z_C$. A mixed s/p-wave tip with a fixed s/p-ratio of 2.5/1 is used in the simulations (see Methods for details). Image sizes 3.0 nm × 1.5 nm.

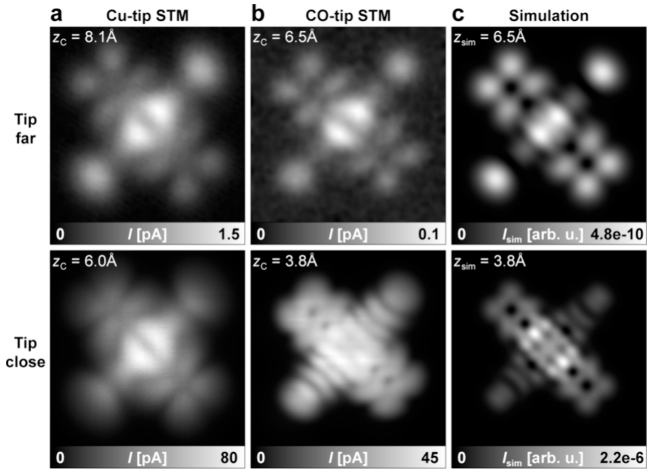

Figure 4. STM of naphthalocyanine on bilayer NaCl/Cu(111). (a) Constant-height STM data at the NIR (V = +0.55 V) measured with a metal (Cu) tip, obtained at large (top row) and small (bottom row) tip−sample distances z_C. (b) Constant-height STM data at the NIR (V = +0.6 V) measured with a CO tip. Extended data can be found in Figure S11. (c) Simulated constant-height STM images of the NIR of naphthalocyanine adsorbed on NaCl. The simulations were performed at the AFM calibrated tip−sample distances $z_{sim} = z_C$. A mixed s/p-wave tip with a fixed s/p-ratio of 2.5/1 is used in the simulations (see Methods). Image sizes 2.7 nm × 2.7 nm.

distance (see Figure S8 for extended data). We also obtain good agreement to constant-current STM images by comparison to calculated isosurfaces (constant $|M|^2$), see Figure S9. Based on the comparison of experiments and simulations, we furthermore propose in Figure S10 a simple method to simulate STM images from DFT orbitals using a convolution with a Gaussian kernel,[6,26,45,59] which qualitatively reproduces the distance dependence. The good agreement between measured and simulated STM images support that the distance dependence of the image contrast inherently arises from different decay lengths of tunneling that involves s- and p-wave tip states.

The simulated STM images in Figure 3b have been obtained based on the DFT-calculated LUMO of pentacene on bilayer NaCl (see Methods). A description of charge transitions accounting for the multireference character of states can be given within the concept of Dyson orbitals.[63] Dyson orbitals describe transitions between molecular N- and $(N \pm 1)$-electron wave functions and capture electronic many-body effects.[64] Depending on the system, shapes and relative energies of Dyson orbitals might differ from the one-electron wave functions.[19,65,66] For the case of pentacene, the highest occupied molecular orbital (HOMO) and LUMO well resemble the shape of their corresponding Dyson orbitals, *i.e.*, for electron detachment and attachment to the neutral molecule, respectively, which allows us to base our analysis on single-reference DFT.[63] Note that for longer acenes such as tridecacene, the multireference character of states becomes more pronounced and needs to be considered.[67,68]

To corroborate the generality of our findings, we measured STM images at different z_C at the NIR of naphthalocyanine, whose LUMO exhibits more nodal planes than that of pentacene.[28,36] With a Cu (s-wave) tip, as for pentacene, STM imaging at "far" and "close" tip−sample distances reveals only minor quantitative, but no qualitative change of contrast (see Figure 4a and extended data in Figure S11). Figure 4b demonstrates the pronounced distance dependence of a CO tip. At small z_C (tip close, bottom image in Figure 4b), the image is predominated by p-wave tip contrast that gives rise to current maxima at the nodal planes of the LUMO.[36] Upon tip retraction to larger distances (tip far, top image in Figure 4b, for extended data see Figure S11), an s-wave tip contrast evolves, which well resembles the one obtained with the Cu (s-wave) tip (Figure 4a). Simulated STM images obtained at the experimentally determined tip heights and using a fixed s/p-ratio of 2.5/1 for the tip states reproduce the experimental CO-tip STM images well over the explored z-range (Figure 4c). These observations are in line with the findings on pentacene, explained by tunneling *via* p-wave tip states decaying steeper than tunneling *via* s-wave tip states, which results in a transition from p-wave to s-wave tip contrast with increasing tip−sample distance.

We emphasize that the s/p-ratio used in the simulations is solely determined to best fit the data and depends on the chosen values of the wave function prefactors and decay constant λ (see Methods). Here, we observe that for both molecules and different individual CO tips, an s/p-ratio of 2.5/1 provides good agreement to the measured STM images at all accessible tip heights (further ratios are shown in Figures S8 and S12 for pentacene and naphthalocyanine, respectively). Finding the same ratio of 2.5/1 for different molecules and different individual tips indicates that the ratio might be applicable to simulate CO-tip STM images also of other molecules.

The accessibility of tip heights for the predominant p-wave tip contrast regime, transition regime, and predominant s-wave tip contrast regime using a CO tip depends on the applicable and measurable tunneling currents. These constraints are more restricting when imaging the PIR of pentacene (V = −2.3 V). Corresponding STM data, $I(z_C)$ curves and discussion can be found in Figures S2 and S3 and Supplementary Note 1, respectively. The CO-tip STM images at the PIR exhibit pronounced p-wave tip character for small tip−sample distances and a mixed s- and p-wave tip contrast in the intermediate regime, as observed for the NIR. However, the

https://doi.org/10.1021/acsnano.4c14476
ACS Nano XXXX, XXX, XXX−XXX

signal at the PIR diminishes before recovering a predominant *s*-wave tip contrast upon further tip retraction.

In our measurements, the apparent onsets at the NIR shift by less than ±50 meV upon changing the tip−sample distance. For pentacene, this can be seen in the STM images in which contrast related to the NIR starts to arise at about V = +1.3 V for all tip heights, for both CO and Cu tips (Figure 1c and Figure S4). Because of the small shift, we discuss the distance dependence of the STM contrast at constant bias voltages (V = +1.4 V for pentacene in Figure 3a, V = +0.6 V for naphthalocyanine in Figure 4b). In general, changing the tip−sample distance can lead to substantial shifts of the ion resonances, *i.e.*, the voltage of the peaks in dI/dV.[61,69,70] This shift mainly results from the tip-height-dependent voltage drop across NaCl (lever arm) and from electron−vibron coupling.[45] We provide a discussion of effects that can lead to shifts in the resonance's peak and onset voltages in Supplementary Note 3.

A CO molecule at the tip apex is subject to substantial geometric relaxations (tilting) in the regime of bond-resolved imaging with AFM, which emerges for about z_C < 3.9 Å (Figure S1). The tilting can significantly affect the image contrast both in STM and AFM.[44,52,71−73] However, in our CO-tip STM measurements (Figure 1c), which are conducted at larger tip−sample distances compared to typical distances for bond-resolved AFM ($z_C \approx 3.5$ Å),[52] we observe no distortions or sharp features in the images in the range of probed tip−sample distances (z_C = [3.6; 9.0] Å). We therefore neglected CO tilting effects in our analysis. We assume that in general, in STM images at ion resonances, the currents will be too large for stable imaging at tip heights at which images are strongly affected by tip relaxations. This assumption is supported by the good agreement of experimental and simulated images (Figure 3), which do not take CO-tip relaxations into account.

Our findings, obtained on ultrathin insulating films and using the current as signal, also qualitatively explain the distance dependence of orbital imaging by dI/dV mapping on metals using CO tips.[39] Based on the feature that the mixing ratio of *s*- and *p*-wave tip states in the simulations does not depend on the tip−sample distance, our proposed method for simulating STM images should be well applicable also to nonplanar molecules.

CONCLUSIONS

In conclusion, we investigated the distance- and voltage-dependent contrast of CO-tip STM images at molecular ion resonances. We observe a crossover from *p*-wave tip contrast (tip "close") to *s*-wave tip contrast (tip "far") upon increasing the tip−sample distance, and only minor contrast variation as a function of the voltage. AFM allowed calibration of the absolute tip−sample distances in experiment, used to define tip heights in simulated STM images. Good agreement between experiment and theory is obtained within a conventional Bardeen approach using a fixed ratio of *s*- to *p*-wave tip states, which inherently reproduces the contrast evolution as a function of tip height. We find that the distance-dependent change of contrast is due to different decay lengths for tunneling between *s*- and *p*-wave-like centers. Our results clarify the resulting image contrast in CO-tip STM of frontier molecular states, which facilitates the comparison of experimental results to *ab initio* calculations.

METHODS

STM and AFM Experiments. STM measurements were performed in a home-built combined STM/AFM setup[35,74] using a qPlus sensor,[75] operated at a temperature of 5 K and a base pressure below 1 × 10^{-10} mbar. The Cu(111) single crystal surface was prepared by repeated cycles of sputtering with Ne ions and annealing to 770 K. NaCl was evaporated onto the crystal surface with the sample held at 280−290 K, resulting in partial coverage with (100)-terminated bilayer NaCl islands. Pentacene and naphthalocyanine molecules were sublimed onto the cold (T < 14 K) sample surface. All data were recorded on molecules adsorbed on bilayer NaCl islands. The bias voltage V was applied to the sample with respect to the tip. The PtIr tip was covered with copper by repeated indentation into the sample surface and functionalized by picking up a CO molecule from NaCl.[35,51]

The AFM was operated in the frequency-modulation mode[76] with the oscillation amplitude kept constant at 0.5 Å. AFM frequency shift versus distance spectroscopy, performed in conjunction with the STM measurements, allowed us to calibrate the tip height z_C and quantify the atomic tip−sample distances of the STM measurements,[52,53] see Figure S1 for more details.

DFT Calculations. The molecular states of pentacene in gas phase (Figure 2a and Figures S3a and S6a) were calculated by means of density functional theory (DFT) using the Psi4 code,[77] utilizing the B3LYP hybrid functional[78] and the 6-31G basis set.

To accurately model the molecular states of surface-adsorbed pentacene to simulate the STM images (Figure 3b and Figures S8, S9b, and S10), we place pentacene on a slab of two layers of NaCl (7 × 7 unit cells), respectively. The atomic positions of the bottom layer are fixed. Pentacene is placed with its center positioned above a Cl atom and its carbon backbone pointing along a Cl row.[27,59] Naphthalocyanine (Figure 4c and Figure S12) is placed with its center positioned above a Cl atom[79] and its naphthalene units pointing along the [001] and [010] directions of two layers of NaCl (10 × 10 unit cells).

The geometries have been optimized using the CP2K 9.1 code,[80] which utilizes the Gaussian Plane Wave method,[81] as implemented in AiiDAlab.[82] The calculations were performed with the PBE functional,[83] including the DFT-D3 van-der-Waals correction[84] and the TZV2P-MOLOPT-GTH basis set.

To estimate the O−C and C−Cu bond lengths in a CO-functionalized Cu tip, a calculation of CO attached to two Cu atoms was performed (CP2K 9.1, PBE-D3, TZV2P-MOLOPT-GTH).[52] The resulting bond lengths are 1.15 Å (O−C) and 1.83 Å (C−Cu), leading to a total distance of 2.98 Å between the foremost Cu-tip atom and O. This agrees well with a measurement of the Cu−O distance of CO adsorbed on a Cu(100) surface, which was reported to be 3.05 ± 0.14 Å.[85]

Simulation of STM Images. For the simulations we employed Bardeen's tunneling theory,[54,55] in which the elastic tunneling current $I \propto |M|^2$ depends on the tunneling matrix element

$$M_{\psi_{tip}-\psi_{mol}} = \iint_S (\psi_{tip}\nabla\psi_{mol} - \psi_{mol}\nabla\psi_{tip})dS$$

Here, all constant prefactors were set to unity. The tip wave functions $\psi_{tip}(\vec{r})$ were modeled using the solutions of the vacuum Schrödinger equation $-\Delta\psi_{s/p_x/p_y}(\vec{r}) = E\psi_{s/p_x/p_y}(\vec{r})$, where *s*, p_x and p_y denote the solutions of *s*- and *p*-like character:[47,54]

$$\psi_s(\vec{r}) = C_s \frac{1}{\lambda r\sqrt{4\pi}} e^{-\lambda r}$$

$$\psi_{px}(\vec{r}) = C_{px}\frac{\sqrt{3}}{\sqrt{4\pi}}\left(\frac{1}{\lambda r} + \frac{1}{\lambda^2 r^2}\right)\frac{x}{r}e^{-\lambda r}$$

$$\psi_{py}(\vec{r}) = C_{py}\frac{\sqrt{3}}{\sqrt{4\pi}}\left(\frac{1}{\lambda r} + \frac{1}{\lambda^2 r^2}\right)\frac{y}{r}e^{-\lambda r}$$

Here, $r = |\vec{r} - \vec{r}_0|$ is the distance to the origin $\vec{r}_0$ of the tip's wave function, x and y are the two Cartesian vector components of $\vec{r} - \vec{r}_0$ in

https://doi.org/10.1021/acsnano.4c14476
ACS Nano XXXX, XXX, XXX−XXX

the surface plane and C_i are normalization constants. We set $C_i = 1$ for simplicity. It has been shown that the *s*-like tip states in a CO tip are well described by a superposition of *s*- and p_z-like wave functions that are centered at the oxygen atom of the CO.[44] If tilting of the CO can be neglected, which is the case at our measurement parameters, both *s*- and p_z-wave tip states exhibit a radially symmetric intensity distribution in the *x*-*y*-plane. We therefore approximate the *s*-wave tip states by a single *s*-wave state ψ_s. Note that qualitatively similar results compared to those discussed in this work can be obtained by modeling the tip using atomic (hydrogen) wave functions.

To calculate the symmetry-dependent decay of the tunneling current (Figure 2f) we used ψ_s (ψ_{px}) for both ψ_{tip} and ψ_{mol} in M_{s-s} (M_{p-p}), and $\lambda = 1.0$ Å^{-1}.

To simulate the STM images of the NIR of pentacene (Figures 3b, S8, S9b and S10) and naphthalocyanine (Figures 4c and S12) we used the molecule- and resonance-specific decay constants $\lambda_{pentacene} = 1.02$ Å^{-1} and $\lambda_{naphthalo} = 1.19$ Å^{-1} for the tip wave functions, respectively. The values were chosen identical to the measured tunneling decay constants at the NIR of pentacene (+1.35 V, Figure 2c) and naphthalocyanine (+0.6 V) by recording $I(z_C)$ with a CO tip placed above a local *s*-like site, because λ is expected to depend on the tunneling barrier height and therefore on the applied voltage: A smaller voltage of the resonance relates to a larger tunneling barrier for the elastic tunneling path between tip and molecule, which implies a faster decay and hence a larger λ. This is in line with the larger λ observed for electron attachment to naphthalocyanine at +0.6 V compared to that to pentacene at +1.35 V. The usage of a voltage-dependent λ thus accounts for the specific tunneling barrier height, which is not captured by considering only the elastic tunneling matrix element $M_{tip\text{-}mol}$.

For the sample wave function ψ_{mol} we used the LUMO and HOMO orbitals as obtained from DFT. While the molecular plane was fixed at a height of $z = 0$, the centers of the tip wave functions were placed to $\vec{r}_0 = (x_0, y_0, z_0)$ above the molecule, which simulates the position of the foremost tip atom (Cu for the Cu tip, O for the CO tip).[44] The tunneling current was then calculated as

$$I(\vec{r}_0) = w_s |M_{\psi_s - \psi_{mol}}|^2 + w_p(|M_{\psi_{px} - \psi_{mol}}|^2 + |M_{\psi_{py} - \psi_{mol}}|^2)$$

with relative contributions w_s and w_p. Note that the *p*-wave contribution is a superposition of $M_{\psi_{px} - \psi_{mol}}$ and $M_{\psi_{py} - \psi_{mol}}$, which accounts for the two degenerate *p*-wave $2\pi^*$ states of CO.[36] Bardeen's integral is evaluated on a plane *S* at $(x, y, z = z_0/2)$. A metal (*s*-wave) tip is simulated using $w_s = 1$ and $w_p = 0$, *p*-wave tunneling is characterized by $w_s = 0$ and $w_p = 1$. For a mixed *s*/*p*-wave CO tip we used fixed contributions $w_s = 2.5$ and $w_p = 1.0$ (ratio 2.5/1) to simulate the CO-tip measurements on pentacene (Figures 3b, S8e and S9b) and naphthalocyanine (Figures 4c and S12). We emphasize that the ratio w_s/w_p is solely determined to best fit the data and depends on the chosen values of the wave function prefactors C_i (here set to 1 for simplicity)[47] and decay constant λ. This, however, does not affect the crucial observation that a *fixed* ratio of w_s/w_p reproduces the experiments well for different tip–sample distances, although the same decay constant λ is used in *s*- and *p*-wave wave functions.

Note that vacuum tip wave functions exhibit an increasing full width at half-maximum in the *xy*-plane with growing distance (in *z*-direction) from their center. The distance-dependent broadening of orbital-density features, *i.e.*, the decrease of the lateral resolution with larger tip–sample distances, is thus inherently included in our calculations.[58,86] Accordingly, no additional broadening of the STM images has been applied.

It is worth noting that Bardeen's tunneling theory only holds if the wave functions of sample and tip do not overlap strongly, *i.e.*, only for sufficiently large tip–sample distances.[55] On the other hand, localized-basis DFT calculations exhibit poor wave function accuracy far away from the molecule's nuclei.[38,46] In addition, the description of the tip using vacuum wave functions neglects microscopic details of the metallic tip apex. We furthermore neglect interference effects between different tip orbitals.[44,87] Nevertheless, we emphasize that our simulations provide excellent agreement between experimental data and calculated constant-height STM images over roughly four orders of magnitude of the tunneling current, covering typical tip–sample distances of experiments.

ASSOCIATED CONTENT

Supporting Information

The Supporting Information is available free of charge at https://pubs.acs.org/doi/10.1021/acsnano.4c14476.

Calibration of the tip–sample distance, additional STM data, and simulations and discussion for the NIR and PIR of pentacene and naphthalocyanine (PDF)

AUTHOR INFORMATION

Corresponding Author

Leo Gross − *IBM Research Europe − Zurich, 8803 Rüschlikon, Switzerland;* orcid.org/0000-0002-5337-4159; Email: LGR@zurich.ibm.com

Authors

Fabian Paschke − *IBM Research Europe − Zurich, 8803 Rüschlikon, Switzerland;* orcid.org/0000-0002-9710-170X

Leonard-Alexander Lieske − *IBM Research Europe − Zurich, 8803 Rüschlikon, Switzerland*

Florian Albrecht − *IBM Research Europe − Zurich, 8803 Rüschlikon, Switzerland;* orcid.org/0000-0002-7418-9155

C. Julian Chen − *Department of Applied Physics and Applied Mathematics, Columbia University, New York, New York 10027, United States*

Jascha Repp − *Institute of Experimental and Applied Physics, University of Regensburg, Regensburg 93053, Germany;* orcid.org/0000-0003-2883-7083

Complete contact information is available at: https://pubs.acs.org/10.1021/acsnano.4c14476

Author Contributions

#F.P. and L.-A.L. contributed equally. L.G. and F.A. conceived the experiment. F.P. and L.-A.L. performed the STM/AFM experiments, DFT modeling, and STM simulations. All authors discussed the results and contributed to writing the manuscript.

Notes

The authors declare no competing financial interest.

ACKNOWLEDGMENTS

We thank S. Mishra for discussions. This work was supported financially by the European Research Council Synergy grant MolDAM (grant no. 951519) and the H2020-MSCA-ITN ULTIMATE (grant no. 813036).

REFERENCES

(1) Grill, L.; Dyer, M.; Lafferentz, L.; Persson, M.; Peters, M. V.; Hecht, S. Nano-Architectures by Covalent Assembly of Molecular Building Blocks. *Nat. Nanotechnol.* **2007**, *2* (11), 687–691.

(2) Pavliček, N.; Gross, L. Generation, Manipulation and Characterization of Molecules by Atomic Force Microscopy. *Nat. Rev. Chem.* **2017**, *1* (1), No. 0005.

(3) Clair, S.; de Oteyza, D. G. Controlling a Chemical Coupling Reaction on a Surface: Tools and Strategies for On-Surface Synthesis. *Chem. Rev.* **2019**, *119* (7), 4717–4776.

(4) Grill, L.; Hecht, S. Covalent On-Surface Polymerization. *Nat. Chem.* **2020**, *12* (2), 115–130.

(5) Cai, J.; Ruffieux, P.; Jaafar, R.; Bieri, M.; Braun, T.; Blankenburg, S.; Muoth, M.; Seitsonen, A. P.; Saleh, M.; Feng, X.; Müllen, K.; Fasel, R. Atomically Precise Bottom-up Fabrication of Graphene Nanoribbons. *Nature* **2010**, *466* (7305), 470−473.
(6) Pavliček, N.; Mistry, A.; Majzik, Z.; Moll, N.; Meyer, G.; Fox, D. J.; Gross, L. Synthesis and Characterization of Triangulene. *Nat. Nanotechnol.* **2017**, *12* (4), 308−311.
(7) Mishra, S.; Beyer, D.; Eimre, K.; Liu, J.; Berger, R.; Gröning, O.; Pignedoli, C. A.; Müllen, K.; Fasel, R.; Feng, X.; Ruffieux, P. Synthesis and Characterization of π-Extended Triangulene. *J. Am. Chem. Soc.* **2019**, *141* (27), 10621−10625.
(8) Mishra, S.; Fatayer, S.; Fernández, S.; Kaiser, K.; Peña, D.; Gross, L. Nonbenzenoid High-Spin Polycyclic Hydrocarbons Generated by Atom Manipulation. *ACS Nano* **2022**, *16* (2), 3264−3271.
(9) Turco, E.; Bernhardt, A.; Krane, N.; Valenta, L.; Fasel, R.; Juríček, M.; Ruffieux, P. Observation of the Magnetic Ground State of the Two Smallest Triangular Nanographenes. *JACS Au* **2023**, *3* (5), 1358−1364.
(10) Kaiser, K.; Scriven, L. M.; Schulz, F.; Gawel, P.; Gross, L.; Anderson, H. L. An Sp-Hybridized Molecular Carbon Allotrope, Cyclo[18]Carbon. *Science* **2019**, *365* (6459), 1299−1301.
(11) Gao, Y.; Albrecht, F.; Rončević, I.; Ettedgui, I.; Kumar, P.; Scriven, L. M.; Christensen, K. E.; Mishra, S.; Righetti, L.; Rossmannek, M.; Tavernelli, I.; Anderson, H. L.; Gross, L. On-Surface Synthesis of a Doubly Anti-Aromatic Carbon Allotrope. *Nature* **2023**, *623*, 977−981.
(12) Sun, L.; Zheng, W.; Gao, W.; Kang, F.; Zhao, M.; Xu, W. On-Surface Synthesis of Aromatic Cyclo[10]Carbon and Cyclo[14]-Carbon. *Nature* **2023**, *623* (7989), 972−976.
(13) Sun, L.; Zheng, W.; Kang, F.; Gao, W.; Wang, T.; Gao, G.; Xu, W. On-Surface Synthesis and Characterization of Anti-Aromatic Cyclo[12]Carbon and Cyclo[20]Carbon. *Nat. Commun.* **2024**, *15* (1), 7649.
(14) Albrecht, F.; Rončević, I.; Gao, Y.; Paschke, F.; Baiardi, A.; Tavernelli, I.; Mishra, S.; Anderson, H. L.; Gross, L. The Odd-Number Cyclo[13]Carbon and Its Dimer, Cyclo[26]Carbon. *Science* **2024**, *384* (6696), 677−682.
(15) Zhong, Q.; Hu, Y.; Niu, K.; Zhang, H.; Yang, B.; Ebeling, D.; Tschakert, J.; Cheng, T.; Schirmeisen, A.; Narita, A.; Müllen, K.; Chi, L. Benzo-Fused Periacenes or Double Helicenes? Different Cyclodehydrogenation Pathways on Surface and in Solution. *J. Am. Chem. Soc.* **2019**, *141* (18), 7399−7406.
(16) Fan, Q.; Martin-Jimenez, D.; Ebeling, D.; Krug, C. K.; Brechmann, L.; Kohlmeyer, C.; Hilt, G.; Hieringer, W.; Schirmeisen, A.; Gottfried, J. M. Nanoribbons with Nonalternant Topology from Fusion of Polyazulene: Carbon Allotropes beyond Graphene. *J. Am. Chem. Soc.* **2019**, *141* (44), 17713−17720.
(17) Biswas, K.; Soler, D.; Mishra, S.; Chen, Q.; Yao, X.; Sánchez-Grande, A.; Eimre, K.; Mutombo, P.; Martín-Fuentes, C.; Lauwaet, K.; Gallego, J. M.; Ruffieux, P.; Pignedoli, C. A.; Müllen, K.; Miranda, R.; Urgel, J. I.; Narita, A.; Fasel, R.; Jelínek, P.; Écija, D. Steering Large Magnetic Exchange Coupling in Nanographenes near the Closed-Shell to Open-Shell Transition. *J. Am. Chem. Soc.* **2023**, *145* (5), 2968−2974.
(18) Jacobse, P. H.; Daugherty, M. C.; Čerņevičs, K.; Wang, Z.; McCurdy, R. D.; Yazyev, O. V.; Fischer, F. R.; Crommie, M. F. Five-Membered Rings Create Off-Zero Modes in Nanographene. *ACS Nano* **2023**, *17* (24), 24901−24909.
(19) Song, S.; Pinar Solé, A.; Matěj, A.; Li, G.; Stetsovych, O.; Soler, D.; Yang, H.; Telychko, M.; Li, J.; Kumar, M.; Chen, Q.; Edalatmanesh, S.; Brabec, J.; Veis, L.; Wu, J.; Jelinek, P.; Lu, J. Highly Entangled Polyradical Nanographene with Coexisting Strong Correlation and Topological Frustration. *Nat. Chem.* **2024**, *16*, 938−944.
(20) Mishra, S.; Melidonie, J.; Eimre, K.; Obermann, S.; Gröning, O.; Pignedoli, C. A.; Ruffieux, P.; Feng, X.; Fasel, R. On-Surface Synthesis of Super-Heptazethrene. *Chem. Commun.* **2020**, *56* (54), 7467−7470.
(21) Turco, E.; Mishra, S.; Melidonie, J.; Eimre, K.; Obermann, S.; Pignedoli, C. A.; Fasel, R.; Feng, X.; Ruffieux, P. On-Surface Synthesis and Characterization of Super-Nonazethrene. *J. Phys. Chem. Lett.* **2021**, *12* (34), 8314−8319.
(22) Mishra, S.; Vilas-Varela, M.; Fatayer, S.; Albrecht, F.; Peña, D.; Gross, L. Observation of SOMO-HOMO Inversion in a Neutral Polycyclic Conjugated Hydrocarbon. *ACS Nano* **2024**, *18* (24), 15898−15904.
(23) Kawai, S.; Takahashi, K.; Ito, S.; Pawlak, R.; Meier, T.; Spijker, P.; Canova, F. F.; Tracey, J.; Nozaki, K.; Foster, A. S.; Meyer, E. Competing Annulene and Radialene Structures in a Single Anti-Aromatic Molecule Studied by High-Resolution Atomic Force Microscopy. *ACS Nano* **2017**, *11* (8), 8122−8130.
(24) Majzik, Z.; Pavliček, N.; Vilas-Varela, M.; Pérez, D.; Moll, N.; Guitián, E.; Meyer, G.; Peña, D.; Gross, L. Studying an Antiaromatic Polycyclic Hydrocarbon Adsorbed on Different Surfaces. *Nat. Commun.* **2018**, *9* (1), 1198.
(25) Schuler, B.; Fatayer, S.; Mohn, F.; Moll, N.; Pavliček, N.; Meyer, G.; Peña, D.; Gross, L. Reversible Bergman Cyclization by Atomic Manipulation. *Nature Chem.* **2016**, *8* (3), 220−224.
(26) Albrecht, F.; Fatayer, S.; Pozo, I.; Tavernelli, I.; Repp, J.; Peña, D.; Gross, L. Selectivity in Single-Molecule Reactions by Tip-Induced Redox Chemistry. *Science* **2022**, *377* (6603), 298−301.
(27) Repp, J.; Meyer, G.; Stojković, S. M.; Gourdon, A.; Joachim, C. Molecules on Insulating Films: Scanning-Tunneling Microscopy Imaging of Individual Molecular Orbitals. *Phys. Rev. Lett.* **2005**, *94* (2), No. 026803.
(28) Liljeroth, P.; Repp, J.; Meyer, G. Current-Induced Hydrogen Tautomerization and Conductance Switching of Naphthalocyanine Molecules. *Science* **2007**, *317* (5842), 1203−1206.
(29) Repp, J.; Meyer, G.; Paavilainen, S.; Olsson, F. E.; Persson, M. Imaging Bond Formation Between a Gold Atom and Pentacene on an Insulating Surface. *Science* **2006**, *312* (5777), 1196−1199.
(30) Mohn, F.; Repp, J.; Gross, L.; Meyer, G.; Dyer, M. S.; Persson, M. Reversible Bond Formation in a Gold-Atom−Organic-Molecule Complex as a Molecular Switch. *Phys. Rev. Lett.* **2010**, *105* (26), No. 266102.
(31) Uhlmann, C.; Swart, I.; Repp, J. Controlling the Orbital Sequence in Individual Cu-Phthalocyanine Molecules. *Nano Lett.* **2013**, *13* (2), 777−780.
(32) Patera, L. L.; Queck, F.; Scheuerer, P.; Repp, J. Mapping Orbital Changes upon Electron Transfer with Tunnelling Microscopy on Insulators. *Nature* **2019**, *566* (7743), 245−248.
(33) Yu, P.; Kocić, N.; Repp, J.; Siegert, B.; Donarini, A. Apparent Reversal of Molecular Orbitals Reveals Entanglement. *Phys. Rev. Lett.* **2017**, *119* (5), No. 056801.
(34) Mishra, S.; Vilas-Varela, M.; Lieske, L.-A.; Ortiz, R.; Fatayer, S.; Rončević, I.; Albrecht, F.; Frederiksen, T.; Peña, D.; Gross, L. Bistability between π-Diradical Open-Shell and Closed-Shell States in Indeno[1,2-a]Fluorene. *Nat. Chem.* **2024**, *16*, 755−761.
(35) Gross, L.; Mohn, F.; Moll, N.; Liljeroth, P.; Meyer, G. The Chemical Structure of a Molecule Resolved by Atomic Force Microscopy. *Science* **2009**, *325* (5944), 1110−1114.
(36) Gross, L.; Moll, N.; Mohn, F.; Curioni, A.; Meyer, G.; Hanke, F.; Persson, M. High-Resolution Molecular Orbital Imaging Using a p -Wave STM Tip. *Phys. Rev. Lett.* **2011**, *107* (8), No. 086101.
(37) Rohlfing, M.; Temirov, R.; Tautz, F. S. Adsorption Structure and Scanning Tunneling Data of a Prototype Organic-Inorganic Interface: PTCDA on Ag(111). *Phys. Rev. B* **2007**, *76* (11), No. 115421.
(38) Gustafsson, A.; Okabayashi, N.; Peronio, A.; Giessibl, F. J.; Paulsson, M. Analysis of STM Images with Pure and CO-Functionalized Tips: A First-Principles and Experimental Study. *Phys. Rev. B* **2017**, *96* (8), No. 085415.
(39) Martinez-Castro, J.; Bolat, R.; Fan, Q.; Werner, S.; Arefi, H. H.; Esat, T.; Sundermeyer, J.; Wagner, C.; Michael Gottfried, J.; Temirov, R.; Ternes, M.; Stefan Tautz, F. Disentangling the Electronic Structure of an Adsorbed Graphene Nanoring by Scanning Tunneling Microscopy. *Commun. Mater.* **2022**, *3* (1), 1−9.

https://doi.org/10.1021/acsnano.4c14476
ACS Nano XXXX, XXX, XXX−XXX

(40) Néel, N.; Kröger, J. Orbital and Skeletal Structure of a Single Molecule on a Metal Surface Unveiled by Scanning Tunneling Microscopy. *J. Phys. Chem. Lett.* **2023**, *14* (16), 3946−3952.
(41) Piquero-Zulaica, I.; Corral-Rascón, E.; Diaz de Cerio, X.; Riss, A.; Yang, B.; Garcia-Lekue, A.; Kher-Elden, M. A.; Abd El-Fattah, Z. M.; Nobusue, S.; Kojima, T.; Seufert, K.; Sakaguchi, H.; Auwärter, W.; Barth, J. V. Deceptive Orbital Confinement at Edges and Pores of Carbon-Based 1D and 2D Nanoarchitectures. *Nat. Commun.* **2024**, *15* (1), 1062.
(42) Odobesko, A.; Klees, R. L.; Friedrich, F.; Hankiewicz, E. M.; Bode, M. Boosting Spatial and Energy Resolution in STM with a Double-Functionalized Probe. *Science. Advances* **2024**, *10* (35), No. eadq6975.
(43) Néel, N.; Dreßler, C.; Kröger, J. Effect of Orbital Symmetry on Probing the Single-Molecule Kondo Effect. *Phys. Rev. B* **2024**, *109* (24), No. L241401.
(44) Abilio, I.; Néel, N.; Kröger, J.; Palotás, K. Scanning Tunneling Microscopy Using CO-Terminated Probes with Tilted and Straight Geometries. *Phys. Rev. B* **2024**, *110* (12), No. 125422.
(45) Pavliček, N.; Swart, I.; Niedenführ, J.; Meyer, G.; Repp, J. Symmetry Dependence of Vibration-Assisted Tunneling. *Phys. Rev. Lett.* **2013**, *110* (13), No. 136101.
(46) Gustafsson, A.; Paulsson, M. Scanning Tunneling Microscopy Current from Localized Basis Orbital Density Functional Theory. *Phys. Rev. B* **2016**, *93* (11), No. 115434.
(47) Chen, C. J. Tunneling Matrix Elements in Three-Dimensional Space: The Derivative Rule and the Sum Rule. *Phys. Rev. B* **1990**, *42* (14), 8841−8857.
(48) Xiang, F.; Maisel, S.; Beniwal, S.; Akhmetov, V.; Ruppenstein, C.; Devarajulu, M.; Dörr, A.; Papaianina, O.; Görling, A.; Amsharov, K. Y.; Maier, S. Planar π-Extended Cycloparaphenylenes Featuring an All-Armchair Edge Topology. *Nat. Chem.* **2022**, *14* (8), 871−876.
(49) Sun, K.; Silveira, O. J.; Ma, Y.; Hasegawa, Y.; Matsumoto, M.; Kera, S.; Krejčí, O.; Foster, A. S.; Kawai, S. On-Surface Synthesis of Disilabenzene-Bridged Covalent Organic Frameworks. *Nat. Chem.* **2023**, *15* (1), 136−142.
(50) Custance, O.; Ventura-Macias, E.; Stetsovych, O.; Romero-Muñiz, C.; Shimizu, T. K.; Pou, P.; Abe, M.; Hayashi, H.; Ohkubo, T.; Kawai, S.; Perez, R. Structure and Defect Identification at Self-Assembled Islands of CO2 Using Scanning Probe Microscopy. *ACS Nano* **2024**, *18*, 26759.
(51) Bartels, L.; Meyer, G.; Rieder, K.-H. Controlled Vertical Manipulation of Single CO Molecules with the Scanning Tunneling Microscope: A Route to Chemical Contrast. *Appl. Phys. Lett.* **1997**, *71* (2), 213−215.
(52) Gross, L.; Mohn, F.; Moll, N.; Schuler, B.; Criado, A.; Guitián, E.; Peña, D.; Gourdon, A.; Meyer, G. Bond-Order Discrimination by Atomic Force Microscopy. *Science* **2012**, *337* (6100), 1326−1329.
(53) Schuler, B.; Liu, W.; Tkatchenko, A.; Moll, N.; Meyer, G.; Mistry, A.; Fox, D.; Gross, L. Adsorption Geometry Determination of Single Molecules by Atomic Force Microscopy. *Phys. Rev. Lett.* **2013**, *111* (10), No. 106103.
(54) Chen, C. J. *Introduction to Scanning Tunneling Microscopy*; Oxford University Press: 2021.
(55) Bardeen, J. Tunnelling from a Many-Particle Point of View. *Phys. Rev. Lett.* **1961**, *6* (2), 57−59.
(56) Gottlieb, A. D.; Wesoloski, L. Bardeen's Tunnelling Theory as Applied to Scanning Tunnelling Microscopy: A Technical Guide to the Traditional Interpretation. *Nanotechnology* **2006**, *17* (8), R57.
(57) Grewal, A.; Leon, C. C.; Kuhnke, K.; Kern, K.; Gunnarsson, O. Scanning Tunneling Microscopy for Molecules: Effects of Electron Propagation into Vacuum. *ACS Nano* **2024**, *18* (19), 12158−12167.
(58) Tersoff, J.; Hamann, D. R. Theory of the Scanning Tunneling Microscope. *Phys. Rev. B* **1985**, *31* (2), 805−813.
(59) Hernangómez-Pérez, D.; Schlör, J.; Egger, D. A.; Patera, L. L.; Repp, J.; Evers, F. Reorganization Energy and Polaronic Effects of Pentacene on NaCl Films. *Phys. Rev. B* **2020**, *102* (11), No. 115419.
(60) Albrecht, F.; Fleischmann, M.; Scheer, M.; Gross, L.; Repp, J. Local Tunneling Decay Length and Kelvin Probe Force Spectroscopy. *Phys. Rev. B* **2015**, *92* (23), No. 235443.
(61) Reecht, G.; Krane, N.; Lotze, C.; Zhang, L.; Briseno, A. L.; Franke, K. J. Vibrational Excitation Mechanism in Tunneling Spectroscopy beyond the Franck-Condon Model. *Phys. Rev. Lett.* **2020**, *124* (11), No. 116804.
(62) Mehler, A.; Néel, N.; Bocquet, M.-L.; Kröger, J. Exciting Vibrons in Both Frontier Orbitals of a Single Hydrocarbon Molecule on Graphene. *J. Phys.: Condens. Matter* **2019**, *31* (6), No. 065001.
(63) Mignolet, B.; Kùs, T.; Remacle, F. Imaging Orbitals by Ionization or Electron Attachment: The Role of Dyson Orbitals. In *Imaging and Manipulating Molecular Orbitals*; Grill, L.; Joachim, C., Eds.; Springer: Berlin, Heidelberg, 2013; pp 41−54. .
(64) Ortiz, J. V. Dyson-Orbital Concepts for Description of Electrons in Molecules. *J. Chem. Phys.* **2020**, *153* (7), No. 070902.
(65) Rascon, E. C.; Riss, A.; Matěj, A.; Wiengarten, A.; Mutombo, P.; Soler, D.; Jelinek, P.; Auwärter, W. On-Surface Synthesis of Square-Type Porphyrin Tetramers with Central Antiaromatic Cyclooctatetraene Moiety. *J. Am. Chem. Soc.* **2023**, *145* (2), 967−977.
(66) Schulz, F.; Ijäs, M.; Drost, R.; Hämäläinen, S. K.; Harju, A.; Seitsonen, A. P.; Liljeroth, P. Many-Body Transitions in a Single Molecule Visualized by Scanning Tunnelling Microscopy. *Nature Phys.* **2015**, *11* (3), 229−234.
(67) Ruan, Z.; Schramm, J.; Bauer, J. B.; Naumann, T.; Bettinger, H. F.; Tonner-Zech, R.; Gottfried, J. M. Synthesis of Tridecacene by Multistep Single-Molecule Manipulation. *J. Am. Chem. Soc.* **2024**, *146* (6), 3700−3709.
(68) Zuzak, R.; Kumar, M.; Stoica, O.; Soler-Polo, D.; Brabec, J.; Pernal, K.; Veis, L.; Blieck, R.; Echavarren, A. M.; Jelinek, P.; Godlewski, S. On-Surface Synthesis and Determination of the Open-Shell Singlet Ground State of Tridecacene. *Angew. Chem., Int. Ed.* **2024**, *63* (9), No. e202317091.
(69) Wu, S. W.; Nazin, G. V.; Chen, X.; Qiu, X. H.; Ho, W. Control of Relative Tunneling Rates in Single Molecule Bipolar Electron Transport. *Phys. Rev. Lett.* **2004**, *93* (23), No. 236802.
(70) Imai-Imada, M.; Imada, H.; Miwa, K.; Jung, J.; Shimizu, T. K.; Kawai, M.; Kim, Y. Energy-Level Alignment of a Single Molecule on Ultrathin Insulating Film. *Phys. Rev. B* **2018**, *98* (20), No. 201403.
(71) Hapala, P.; Kichin, G.; Wagner, C.; Tautz, F. S.; Temirov, R.; Jelínek, P. Mechanism of High-Resolution STM/AFM Imaging with Functionalized Tips. *Phys. Rev. B* **2014**, *90* (8), No. 085421.
(72) Boneschanscher, M. P.; Hämäläinen, S. K.; Liljeroth, P.; Swart, I. Sample Corrugation Affects the Apparent Bond Lengths in Atomic Force Microscopy. *ACS Nano* **2014**, *8* (3), 3006−3014.
(73) Neu, M.; Moll, N.; Gross, L.; Meyer, G.; Giessibl, F. J.; Repp, J. Image Correction for Atomic Force Microscopy Images with Functionalized Tips. *Phys. Rev. B* **2014**, *89* (20), No. 205407.
(74) Meyer, G. A Simple Low-temperature Ultrahigh-vacuum Scanning Tunneling Microscope Capable of Atomic Manipulation. *Rev. Sci. Instrum.* **1996**, *67* (8), 2960−2965.
(75) Giessibl, F. J. Atomic Resolution on Si(111)-(7 × 7) by Noncontact Atomic Force Microscopy with a Force Sensor Based on a Quartz Tuning Fork. *Appl. Phys. Lett.* **2000**, *76* (11), 1470−1472.
(76) Albrecht, T. R.; Grütter, P.; Horne, D.; Rugar, D. Frequency Modulation Detection Using high-Q Cantilevers for Enhanced Force Microscope Sensitivity. *J. Appl. Phys.* **1991**, *69* (2), 668−673.
(77) Smith, D. G. A.; Burns, L. A.; Simmonett, A. C.; Parrish, R. M.; Schieber, M. C.; Galvelis, R.; Kraus, P.; Kruse, H.; Di Remigio, R.; Alenaizan, A.; James, A. M.; Lehtola, S.; Misiewicz, J. P.; Scheurer, M.; Shaw, R. A.; Schriber, J. B.; Xie, Y.; Glick, Z. L.; Sirianni, D. A.; O'Brien, J. S.; Waldrop, J. M.; Kumar, A.; Hohenstein, E. G.; Pritchard, B. P.; Brooks, B. R.; Schaefer, H. F.; Sokolov, A. Yu.; Patkowski, K.; DePrince, A. E.; Bozkaya, U.; King, R. A.; Evangelista, F. A.; Turney, J. M.; Crawford, T. D.; Sherrill, C. D. PSI4 1.4: Open-Source Software for High-Throughput Quantum Chemistry. *J. Chem. Phys.* **2020**, *152* (18), No. 184108.
(78) Stephens, P. J.; Devlin, F. J.; Chabalowski, C. F.; Frisch, M. J. Ab Initio Calculation of Vibrational Absorption and Circular

https://doi.org/10.1021/acsnano.4c14476
ACS Nano XXXX, XXX, XXX−XXX

Dichroism Spectra Using Density Functional Force Fields. *J. Phys. Chem.* **1994**, *98* (45), 11623−11627.
(79) Sarhan, A.; Arboleda, N. B., Jr; David, M.; Nakanishi, H.; Kasai, H. STM-Induced Switching of the Hydrogen Molecule in Naphthalocyanine. *J. Phys.: Condens. Matter* **2009**, *21* (6), No. 064201.
(80) Kühne, T. D.; Iannuzzi, M.; Del Ben, M.; Rybkin, V. V.; Seewald, P.; Stein, F.; Laino, T.; Khaliullin, R. Z.; Schütt, O.; Schiffmann, F.; Golze, D.; Wilhelm, J.; Chulkov, S.; Bani-Hashemian, M. H.; Weber, V.; Borštnik, U.; Taillefumier, M.; Jakobovits, A. S.; Lazzaro, A.; Pabst, H.; Müller, T.; Schade, R.; Guidon, M.; Andermatt, S.; Holmberg, N.; Schenter, G. K.; Hehn, A.; Bussy, A.; Belleflamme, F.; Tabacchi, G.; Glöß, A.; Lass, M.; Bethune, I.; Mundy, C. J.; Plessl, C.; Watkins, M.; VandeVondele, J.; Krack, M.; Hutter, J. CP2K: An Electronic Structure and Molecular Dynamics Software Package - Quickstep: Efficient and Accurate Electronic Structure Calculations. *J. Chem. Phys.* **2020**, *152* (19), No. 194103.
(81) Lippert, G.; Hutter, J.; Parrinello, M. A Hybrid Gaussian and Plane Wave Density Functional Scheme. *Mol. Phys.* **1997**, *92* (3), 477−488.
(82) Yakutovich, A. V.; Eimre, K.; Schütt, O.; Talirz, L.; Adorf, C. S.; Andersen, C. W.; Ditler, E.; Du, D.; Passerone, D.; Smit, B.; Marzari, N.; Pizzi, G.; Pignedoli, C. A. AiiDAlab − an Ecosystem for Developing, Executing, and Sharing Scientific Workflows. *Comput. Mater. Sci.* **2021**, *188*, No. 110165.
(83) Perdew, J. P.; Burke, K.; Ernzerhof, M. Generalized Gradient Approximation Made Simple. *Phys. Rev. Lett.* **1996**, *77* (18), 3865−3868.
(84) Grimme, S.; Antony, J.; Ehrlich, S.; Krieg, H. A Consistent and Accurate Ab Initio Parametrization of Density Functional Dispersion Correction (DFT-D) for the 94 Elements H-Pu. *J. Chem. Phys.* **2010**, *132* (15), No. 154104.
(85) Andersson, S.; Pendry, J. B. Structure of CO Adsorbed on Cu(100) and Ni(100). *Phys. Rev. Lett.* **1979**, *43* (5), 363−366.
(86) Sacks, W.; Gauthier, S.; Rousset, S.; Klein, J.; Esrick, M. A. Surface Topography in Scanning Tunneling Microscopy: A Free-Electron Model. *Phys. Rev. B* **1987**, *36* (2), 961−967.
(87) Mándi, G.; Palotás, K. Chen's Derivative Rule Revisited: Role of Tip-Orbital Interference in STM. *Phys. Rev. B* **2015**, *91* (16), No. 165406.

https://doi.org/10.1021/acsnano.4c14476
ACS Nano XXXX, XXX, XXX−XXX